Available online at www.sciencedirect.com

jmr&t Journal of Materials Research and Technology

journal homepage: www.elsevier.com/locate/jmrt

Original Article

Experimental and modeling analysis of p-type $Bi_{0.4}Sb_{1.6}Te_3$ and graphene nanocomposites

Aicha S. Lemine [a,b], *Farah M. El-Makaty* [a,b], *Hana A. Al-Ghanim* [c], *Khaled M. Youssef* [a,*]

[a] *Department of Physics, Materials Science and Technology Graduate Program, Qatar University, Doha, 2713, Qatar*
[b] *Department of Mechanical and Industrial Engineering, Qatar University, Doha, 2713, Qatar*
[c] *Department of Civil and Architectural Engineering, Qatar University, Doha, 2713, Qatar*

ARTICLE INFO

Article history:
Received 2 November 2021
Accepted 20 December 2021
Available online 24 December 2021

Keywords:
Graphene
Bismuth telluride alloys
Thermoelectric conversion
Mechanical synthesis
Modeling

ABSTRACT

The state-of-the-art Bismuth-Telluride (Bi_2Te_3) based systems are promising thermoelectric materials for efficient thermoelectric applications. In this study, the effect of graphene nanosheets (GNS) integrity on thermoelectric properties of a p-type $Bi_{0.4}Sb_{1.6}Te_3$ alloy has been studied using high-energy ball milling and SPS sintering techniques. The synthesized pristine $Bi_{0.4}Sb_{1.6}Te_3$ and 0.05wt% GNS/$Bi_{0.4}Sb_{1.6}Te_3$ nanocomposites at different addition times of GNS have exhibited a single-phase and artifact-free bulk nanocrystalline $Bi_{0.4}Sb_{1.6}Te_3$ with nanocrystals size of 17 nm. The TEM analysis confirmed the mechanical exfoliation of graphene filler in 5m nanocomposite into a single-layered nanostructure with an interplanar spacing of 0.343 nm. The prominent Raman features of the monolayered graphene sheet have appeared in the synthesized 5m-GNS/$Bi_{0.4}Sb_{1.6}Te_3$ nanocomposite. This highlighted the crucial rule of graphene addition time on its structure and morphology of the synthesized nanocomposites. The ZT profile of 5m nanocomposite reached 0.801 at 348 K till 398 K. This resulted in 65% of improvements to the pristine $Bi_{0.4}Sb_{1.6}Te_3$ pellet at 323 K. The obtained results were used to simulate a thermoelectric (TE) device module using ANSYS Workbench. The GNS nanocomposites have shown an ultrahigh output power of 95.57 W compared to 89.96 W for the pristine module at ΔT of 150 °C. The GNS addition has increased the output power of pristine $Bi_{0.4}Sb_{1.6}Te_3$ by 7%, leading to comparable TE performance to other simulated Bi_2Te_3 systems.

1. Introduction

Nowadays, there is a selective investment in thermoelectric (TE) technology due to its unique capability for effective recovering of waste heat from intensive electricity consumption sectors. This recovered thermal energy is converted into useful electrical energy for powering their electronic devices, lowering their operating costs, and minimizing their greenhouse emissions [1]. Many thermoelectric materials have been explored for power generation applications, such as GeTe [2], PbTe [3], half Heuslers [4], Bi_2Te_3 [5], and $MgSi_{1.75}$ [6]. The Bismuth-Telluride (Bi_2Te_3) based TE materials have been studied extensively since the 1950s due to their proven

* Corresponding author.
E-mail address: kyoussef@qu.edu.qa (K.M. Youssef).
https://doi.org/10.1016/j.jmrt.2021.12.096

potentials to be the ideal TE systems for low-temperature applications near room temperature. The atomic doping of Bi_2Te_3-based alloys with Antimony (Sb) is favorable in broadening their bandgap (E_g) to upshift their operating temperature, thermal stability, and service life [7].

The Bismuth Antimony Telluride in the alloying composition of $Bi_{0.4}Sb_{1.6}Te_3$ is reported to have the maximum Figure-of-Merit (ZT) value of 0.51 at 375 K and high thermoelectric conversion efficiencies up to 7.5% [8,9]. The nanostructuring of $Bi_{0.4}Sb_{1.6}Te_3$ ternary alloy further enhanced its TE performance via introducing the Quantum confinement effect in which its grains size will be reduced to nano-size, hence high boundaries scattering for low lattice conductivity. While the energy bands will be converted to discrete energy levels with incremental energy gap, hence the high density of states (DOS) near Fermi level for high Seebeck Coefficient (S) [10]. In this study, the transition from bulk-scale to the nanoscale is attained via the high-energy ball milling (HE-BM) technique.

This technique should strengthen the phonon scattering mechanisms, mainly phonon-boundary and phonon–phonon scatterings. Thus, impeding phonons transport across $Bi_{0.4}Sb_{1.6}Te_3$ without affecting the mobility of its charge carriers [11]. The TE enhancements in $Bi_{0.4}Sb_{1.6}Te_3$ alloys are not limited to phonon transport engineering instead, it includes charge transport engineering. This engineering approach will be considered to overcome the dilemma of interconnectivity between TE properties of $Bi_{0.4}Sb_{1.6}Te_3$ through utilizing their strong reliance on electronic and crystal structures, hence optimizing the electron transport processes [12]. This is attainable via introducing low-dimensionality structured materials (e.g., 2D, 1D, or 0D) into nanostructured bulk $Bi_{0.4}Sb_{1.6}Te_3$ [13].

The compositing of nanostructured $Bi_{0.4}Sb_{1.6}Te_3$ with 2D materials has proven its outstanding TE performance, particularly with the 2D Graphene material [14]. This is due to its exceptional structural and electrical properties, which further enhanced the ZT of the $Bi_{0.4}Sb_{1.6}Te_3$ system [14]. Graphene is characterized as a semiconductor material with zero energy gap due to its lattice structure of 2D honeycomb carbon [15]. Thus, it has a high density of charge carriers that behave like massless relativistic particles and move freely in rapid motions across the monolayer graphene, hence high electrical conductivity of ~106S/cm [16]. This single carbon layer is also reported to have a high crystallinity structure with low defects density [16].

Accordingly, this thinnest sheet with a thickness of one carbon atom well matches the layered crystal structure of the promising $Bi_{0.4}Sb_{1.6}Te_3$ system for TE applications of low temperatures [17]. However, the use of graphene in nanocomposite with $Bi_{0.4}Sb_{1.6}Te_3$ system is limited due to its zero bandgap structure, which lowers S and strong C–C covalent bonds that leads to its high thermal conductivity (k) of ~5000 W/m.K [18]. Thus, the content of this conductive filler in the $Bi_{0.4}Sb_{1.6}Te_3$ metallic matrix should be selected properly to synthesis outstanding $Bi_{0.4}Sb_{1.6}Te_3$/graphene nanocomposites. These nanocomposites should have low thermal conductivity while high electrical conductivity to fulfill the ZT enhancements.

This strong influence of graphene content on the lattice and total thermal conductivities of the BiSbTe system is frequently reported [19]. It is proven that the graphene content of 0.05wt% has the lowest k values for $Bi_{0.48}Sb_{1.52}Te_3$/graphene nanocomposites [19]. Accordingly, it has resulted in their ultra-high ZT values of ~1.26 at 325 K compared to the ZT of ~0.89 for pristine $Bi_{0.48}Sb_{1.52}Te_3$ at the same temperature [19]. This is referred to as the even dispersion of graphene at low contents in nanostructured $Bi_{0.48}Sb_{1.52}Te_3$ matrices, particularly near 0.05wt%. This has also facilitated its charge carrier transfer and raised its interfaces densities for effective phonons scattering.

In this study, we utilized and integrated the phonon and charge transport engineering approaches in investigating the thermoelectric enhancements of $Bi_{0.4}Sb_{1.6}Te_3$/graphene nanocomposites. This is attained via synthesizing samples of pristine $Bi_{0.4}Sb_{1.6}Te_3$ and $Bi_{0.4}Sb_{1.6}Te_3$/graphene nanocomposites. The nanocomposites are synthesized at the same elemental compositions of pristine $Bi_{0.4}Sb_{1.6}Te_3$ and fixed filler weight of 0.05wt % graphene nanosheets (GNS). The time for nanocomposite formation will be optimized by adjusting the time of filler addition (GNS) to the metallic matrix ($Bi_{0.4}Sb_{1.6}Te_3$ nanopowder). Thus, graphene addition time will vary from full time, half time, and last 5min of overall 16hrs of the continuous milling process. The optimized thermoelectric outcomes are then simulated and modeled through ANSYS Workbench software.

2. Experimental

2.1. Samples preparation and processing methods

2.1.1. Synthesis of $Bi_{0.4}Sb_{1.6}Te_3$

The high purity elemental powders of bismuth (99.999%, −200 mesh), antimony (99.999%, −200 mesh), and tellurium (99.99%, −325 mesh) from Alfa Aesar were weighted under an ultra-high purity Argon atmosphere (O_2 < 0.5 ppm) in the fixed atomic composition of $Bi_{0.4}Sb_{1.6}Te_3$ to synthesize the p-type bismuth telluride alloy. The weighted powders were loaded in a stainless-steel vial with a ball-to-powder ratio of 10:1 and milled using the SPEX milling device (SamplePrep, 8000M) for 16 h.

2.1.2. Synthesis of GNS/$Bi_{0.4}Sb_{1.6}Te_3$

GNSs from Sigma–Aldrich with an average of 5–7 atomic layers were used to prepare the GNS/$Bi_{0.4}Sb_{1.6}Te_3$ nanocomposites. Three different batches of the nanocomposites were synthesized to investigate the effect of milling on the structural integrity of GNSs and the equivalent TE properties. In these three batches, the GNS was added in a fixed amount of 0.05 wt.% and at different milling time intervals, as presented in Table 1. The Spark Plasma Sintering (SPS, model: DSP-510) was used under a nitrogen atmosphere for dense consolidation of the milled powders in a 12.7 mm graphite die, uniform temperature of 280 °C, uniaxial pressure of 45 MPa, and holding time of 10 min.

2.2. Characterization techniques

2.2.1. Structural and morphology

The X-ray diffraction (XRD: PANalytical, EMPYREAN) was used for the phase identification of the as milled powder samples using Cu/Kα radiation source and a wavelength of 1.54 Å. The Raman Spectroscopy (RS: Thermo Fisher, DXR) was used to examine the degree of crystallinity and structural defects of GNSs at a wavelength of 532 nm and a laser power of 10 mW.

Table 1 – List of samples prepared at different GNS milling time.

Sample Code	GNS amount (wt.%)	GNS addition time
Pristine $Bi_{0.4}Sb_{1.6}Te_3$	0	–
16h-GNS/$Bi_{0.4}Sb_{1.6}Te_3$	0.05%	at full time, 16 h of milling
8h-GNS/$Bi_{0.4}Sb_{1.6}Te_3$	0.05%	at half time, 8 h of milling
5m-GNS/$Bi_{0.4}Sb_{1.6}Te_3$	0.05%	at last 5 min of milling

The microstructure features and the grain size of the synthesized samples were investigated via Transmission electron microscopy (TEM: Tecnai G2 FEG 200 kV, FEI). The TEM samples were prepared by sonicating in isopropyl alcohol using an Ultrasonicator bath for 20 min. The sonicated material was then drop-casted onto a 300-mesh carbon-film-covered copper gird.

2.2.2. *Thermoelectric properties measurements*

The SBA 485 Nemesis – NETZSCH instrument was used for simultaneous measurements of the Seebeck coefficient and electrical conductivity of the consolidated pellets with 12.7 mm in diameter and 3 mm in thickness. The LFA 467 Hyper Flash device – NETZSCH was used for thermal conductivity measurements. These measurements were conducted under an ultra-high purity Argon atmosphere in a temperature range of 323 K–425 K. The TE measurements for each sample were repeated three times, and the maximum standard deviation was less than 7%.

2.2.3. *ANSYS modeling of pristine and GNS based p-$Bi_{0.4}Sb_{1.6}Te_3$ and n-$Bi_2Te_{2.7}Se_{0.3}$ device*

The TE properties obtained from experimental data were used to simulate a thermoelectric device using ANSYS Workbench. The theory behind the Thermal-Electric system utilized and its basic equations can be found in reference [20]. The dimensions of the designed model are 65 × 34 mm containing 127 pairs of thermocouples connected in series, as demonstrated in Fig. 1a. Figure 1b shows the geometry of a single thermocouple consisting of p- and n-legs covered with copper strips. The legs and strips are sandwiched between two alumina plates. The chosen dimensions are based on several reported models of thermoelectric generators [21,22].

For simulation purposes, the TE properties of the p-type material obtained in this study were considered. For the n-type part, recently published data by our research group for GNS-$Bi_2Te_{2.7}Se_{0.3}$ nanocomposites prepared via the same technique is considered [23]. For comparison purposes, two systems will be simulated using the same model. System 1 is based on pristine $Bi_{0.4}Sb_{1.6}Te_3$ and $Bi_2Te_{2.7}Se_{0.3}$ alloys. While system 2 involves the optimum GNS based samples of 5m-GNS/$Bi_{0.4}Sb_{1.6}Te_3$ and 10m-GNS/$Bi_2Te_{2.7}Se_{0.3}$ nanocomposites. The TE properties for the n- and p-type materials of each system are summarized in Table 2.

The electrical resistivity, thermal conductivity, and Seebeck coefficient are considered to be isotropic. However, the variations of these parameters with temperature are incorporated in the simulations. For the copper strips and alumina plates, built–in properties in the software of these materials were used. The geometry of the overall modeled device is shown in Fig. 2a (the upper alumina plate was removed for better visualization).

The simulations assume steady-state conditions are achieved once a temperature difference is introduced to the system. During simulations, the sink temperature was applied to the bottom surface of the lower alumina plate and kept at 20 °C. Meanwhile, to study the effect of the temperature gradient applied across the device on the resulted output power, various source temperatures were applied and tested (hot temperature is applied on the top surface of the upper alumina plate). The resulting current from the specified conditions was calculated by assuming a 5 Ω load resistance applied to the device's ends (Fig. 2a). For accurate results, the meshing of a single thermocouple is based on 525 nodes and 64 elements with a small element size of 0.007 mm (Fig. 2b).

3. Results and discussions

3.1. *Structural and morphology*

3.1.1. *XRD analysis of pristine $Bi_{0.4}Sb_{1.6}Te_3$ and GNS/$Bi_{0.4}Sb_{1.6}Te_3$ nanocomposites*

The crystallographic structure of the as milled samples of pristine and GNS nanocomposites was examined to evaluate

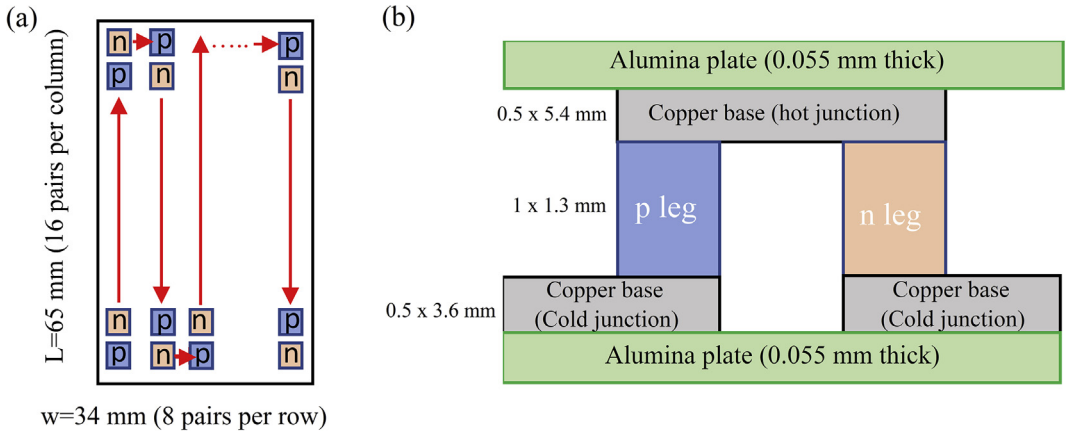

Fig. 1 – Schematics showing the (a) design of simulated TE device, (b) components and geometry of a single thermocouple.

Table 2 – Properties of the TE materials used in the TE module within a temperature range of 50 °C to 150 °C.

Property		p-type	n-type
System 1		pristine $Bi_{0.4}Sb_{1.6}Te_3$	pristine $Bi_2Te_{2.7}Se_{0.3}$
Electrical resistivity	(Ωm)	4.33 E-5 to 4.78 E-5	1.03 E-5 to 1.37 E-5
Thermal conductivity	(W/m.K)	0.85 to 0.99	0.983 to 1.02
Seebeck coefficient	(V/K)	2.31 E-4 to 2.19 E-4	−1.2 E-4 to −1.45 E-4
Density	(g/cm^3)	6.54	7.34
System 2		5m-GNS/$Bi_{0.4}Sb_{1.6}Te_3$	10m-GNS/$Bi_2Te_{2.7}Se_{0.3}$
Electrical resistivity	(Ωm)	2.91 E-5 to 3.41 E-5	7.91 E-6 to 1.06 E-5
Thermal conductivity	(W/m.K)	0.72 to 0.81	1.035 to 1.04
Seebeck coefficient	(V/K)	2.24 E-4 to 2.18 E-4	−1.17 E-4 to −1.44 E-4
Density	(g/cm^3)	6.64	7.26

the adopted preparation and processing methods before their SPS consolidation. The XRD patterns of pristine and nanocomposites show the formation of single-phase $Bi_{0.4}Sb_{1.6}Te_3$ nanocrystals, as displayed in Fig. 3. The characteristic peaks of these XRD patterns are consistent with the standard peaks of rhombohedral $Bi_{0.4}Sb_{1.6}Te_3$ intermetallic compound phase in the Inorganic Crystal Structure Database (ICSD 98-024-7619) [24]. This good agreement in peaks positions and intensities indicates the uniform crystallographic structure of synthesized BiSbTe nanocrystals in pristine and nanocomposite samples.

Figure 3 shows the appearance of Bragg's fundamental peak for this crystalline metallic matrix with an indexed crystal plane of (015) at a low Bragg's angle (2θ) of 28.01° in very strong intensity. It illustrates also the influence of milling time on the graphene distribution and integrity in the p-type BiSbTe matrix. The diffraction peaks of graphene did not appear in the diffraction patterns of synthesized GNS/$Bi_{0.4}Sb_{1.6}Te_3$ nanocomposites, which is attributed to the small amount of the added graphene (0.05wt%).

These low contents of graphene, particularly near 0.05wt% have exhibited even dispersion in $Bi_{0.4}Sb_{1.6}Te_3$ matrices [25]. This will strengthen its doping effect, facilitate its charge carrier transfer, and raise its interfaces densities for effective phonons scattering. Additionally, the broadening in the observed XRD peaks profile of synthesized nanopowders gives a reliable insight on their average crystallites size, which have been quantified using the Warren-Averbach method [26,27]:

$$\frac{\beta_{hkl}{}^2}{\tan^2\theta} = \frac{\lambda}{D}\left(\frac{\beta_{hkl}}{\tan\theta \sin\theta}\right) + 25\,\langle\varepsilon^2\rangle \quad (1)$$

Where β_{hkl} is the FWHM of the peak (hkl) in radian, λ is the wavelength of the x-rays beam, θ is the diffraction angle of the peak in radian, D is the average grains size, and ε is the lattice strain. The calculations of average grains size are based on the highest intensity peaks: (015), (1010), (110), (0210), and (1115). Fitting the data of $\beta_{hkl}^2/\tan^2\theta$ vs $\beta_{hkl}/(\tan\theta \sin\theta)$ through Gaussian function gave the best-fitting linear regression model to all of the recognized diffraction peaks in XRD patterns of either pristine $Bi_{0.4}Sb_{1.6}Te_3$ or GNS/$Bi_{0.4}Sb_{1.6}Te_3$ nanocomposites. This resulted in higher R^2 values of their linear trendlines to be always around 1, which confirms the precision of the drawn and reported conclusions on average grains size of synthesized samples.

The synthesized pristine $Bi_{0.4}Sb_{1.6}Te_3$ shows an average grains size of 17 nm, as displayed in Table 3. These ultrafine nanosized grains of single-phase $Bi_{0.4}Sb_{1.6}Te_3$ are suitable for synthesizing the desired nanostructure of GNS/$Bi_{0.4}Sb_{1.6}Te_3$ nanocomposites. Interestingly, the average grains size for the as milled GNS/$Bi_{0.4}Sb_{1.6}Te_3$ nanocomposites was found to be around 18 nm and then were not considerably affected by changing the time of graphene addition during the mechanical milling process, as shown in Table 3.

3.1.2. *TEM analysis of 5m-GNS/$Bi_{0.4}Sb_{1.6}Te_3$ nanocomposite*

The TEM analysis was conducted on the as milled 5m-GNS/$Bi_{0.4}Sb_{1.6}Te_3$ to confirm the average grains size calculations using the Warren-Averbach and examine the morphology of GNS/$Bi_{0.4}Sb_{1.6}Te_3$ nanocomposites. The TEM analysis shows the formation of $Bi_{0.4}Sb_{1.6}Te_3$ nanocrystals and 2D graphene nanoplatelets within the synthesized 5mins milled GNS/

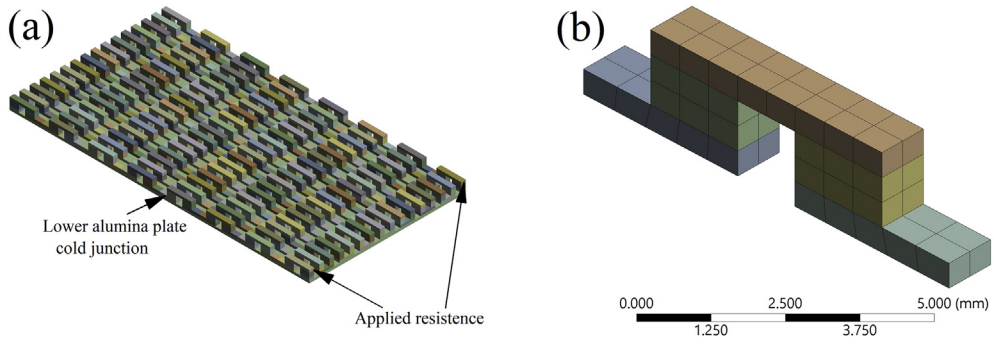

Fig. 2 – (a) The designed TE model using ANSYS Workbench and (b) the meshing of a single thermocouple.

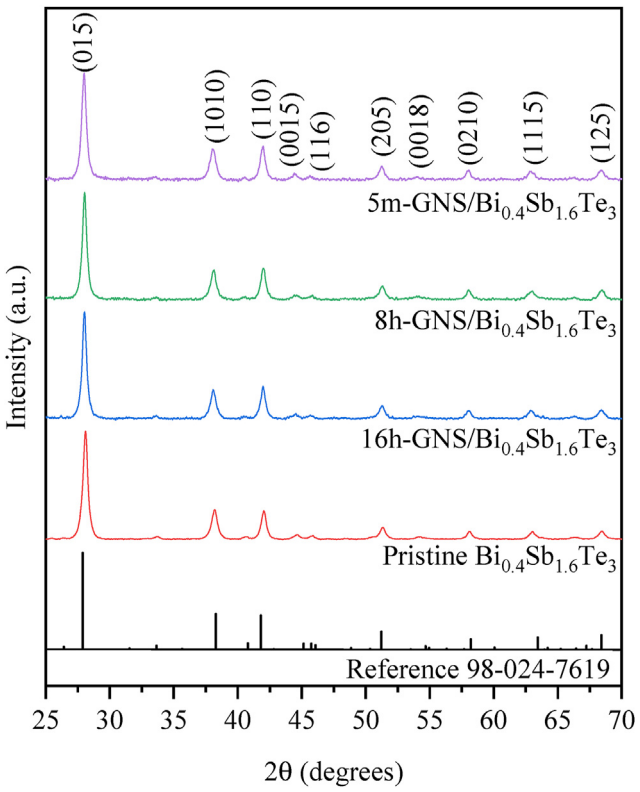

Fig. 3 – The XRD patterns for pristine $Bi_{0.4}Sb_{1.6}Te_3$ and GNS/$Bi_{0.4}Sb_{1.6}Te_3$ nanocomposites.

$Bi_{0.4}Sb_{1.6}Te_3$ nanocomposite, as displayed in Fig. 4a. This figure represents the bright-field (BF) TEM micrograph of 5m-GNS/$Bi_{0.4}Sb_{1.6}Te_3$ nanocomposite. The BF-TEM micrograph of the $Bi_{0.4}Sb_{1.6}Te_3$ matrix shows equiaxed and randomly distributed grains within the nanocomposite structure, as presented in Fig. 4b.

It is observable in the dark-field (DF) TEM micrographs of $Bi_{0.4}Sb_{1.6}Te_3$ matrix that there are uniform grain sizes and distribution without noticing the presence of agglomerated nanocrystallites, as shown in Fig. 4c. This confirms the homogenous solubility of $Bi_{0.4}Sb_{1.6}Te_3$ during the milling process without undergoing welding, which is the main drawback of the mechanical milling technique in synthesizing nanostructured materials [28]. It is noticeable from the Selected Area Diffraction Pattern (SADP) that the observed nanograins in the BF-TEM micrographs are corresponding to the $Bi_{0.4}Sb_{1.6}Te_3$ matrix. It appears to be equiaxed in random orientations, which match their diffraction profile in the XRD patterns, as illustrated in Fig. 4d.

Table 3 – Warren-Averbach calculations of grain size for pristine $Bi_{0.4}Sb_{1.6}Te_3$ and GNS/$Bi_{0.4}Sb_{1.6}Te_3$ nanocomposites.

Sample	Grain size (nm)
$Bi_{0.4}Sb_{1.6}Te_3$	17
16h-GNS/$Bi_{0.4}Sb_{1.6}Te_3$	18
8h-GNS/$Bi_{0.4}Sb_{1.6}Te_3$	19
5m-GNS/$Bi_{0.4}Sb_{1.6}Te_3$	17

The statistical analysis on the DF-TEM micrograph confirms the agreement of the average grains size for the metallic matrix of $Bi_{0.4}Sb_{1.6}Te_3$ nanocrystals within the 5m-GNS/$Bi_{0.4}Sb_{1.6}Te_3$ nanocomposite to their XRD outcomes, as displayed in Fig. 4e. The average grain size in the $Bi_{0.4}Sb_{1.6}Te_3$ matrix is found to be 17 ± 5 nm with no grains above 35 nm based on calculations from several DF-TEM micrographs. This further validates the drawn observations on average grains size using the Warren-Averbach method.

The 2D nanostructure of graphene nanoplatelets in the 5m-GNS/$Bi_{0.4}Sb_{1.6}Te_3$ nanocomposite is observable from its BF and DF TEM micrographs, as displayed in Fig. 4f and g. The SADP of GNS filler in 5m nanocomposite well matches its frequently reported diffraction patterns for single-layered graphene, as illustrated in Fig. 4h [29]. Remarkably, the TEM analysis of graphene filler in 5m-GNS/$Bi_{0.4}Sb_{1.6}Te_3$ nanocomposite confirms its mechanical exfoliation during the high-energy ball milling process [30,31]. It is exfoliated from multi-layered in the as-received GNS powder to single-layered GNS in the 5min nanocomposite, as demonstrated in Fig. 4f. The High-Resolution TEM (HRTEM) micrograph confirms the interplanar spacing of GNS filler as 0.343 nm in 5m-GNS/$Bi_{0.4}Sb_{1.6}Te_3$ nanocomposite, as shown in Fig. 4i. This could maximize the isotropic TE performance of synthesized TE materials for efficient TE energy conversion.

3.1.3. *Raman analysis of GNS/$Bi_{0.4}Sb_{1.6}Te_3$ nanocomposites*

The nanostructure evolution of graphene nanoplatelets in the synthesized samples has been investigated via Raman Spectroscopy. Figure 5 shows the Raman spectra at standard DXR laser excitation of 532 nm to investigate the morphology of graphene in the reference powder (as-received GNS) and synthesized nanocomposites (as-milled GNS). Three main bands appear distinguishably in the Raman spectra of synthesized GNS/$Bi_{0.4}Sb_{1.6}Te_3$ nanocomposites. The first is the D band, representing the level of defects within the carbon lattice [32,33]. The second two are the characteristic bands of graphene, which are the G and 2D bands [34,35]. This investigation is quantified reliably based on calculations of the intensity ratio between the 2D and G bands (I2D/IG ratios) from their Raman spectra.

The outcomes of I_{2D}/I_G ratio calculations confirm the crucial rule of graphene addition time on its structure and morphology of the synthesized nanocomposites, as displayed in Table 4. This table shows the transition trend in the number of graphene layers from multi-to single-layered structures. The multi-layered graphene appears in the as-received GNS, full-time (added initially and undergone 16hrs of milling), and half-time (added after 8hrs and undergone 8hrs of milling) nanocomposites. This multi-layered structure is referred to as the excessive milling of graphene due to its addition at early milling times, which in return affected its unique 2D integrity. The addition of graphene into the last 5mins of the overall 16hrs milling time resulted in a structural transition to single-layered graphene.

This is consistent with the TEM observations on the nanostructure and morphology of 5m-GNS/$Bi_{0.4}Sb_{1.6}Te_3$ nanocomposite. This also draws a direct relationship between GNS's structural integrity and its milling time. Increasing the milling time from 5 min to 16 h led to an elevation in the

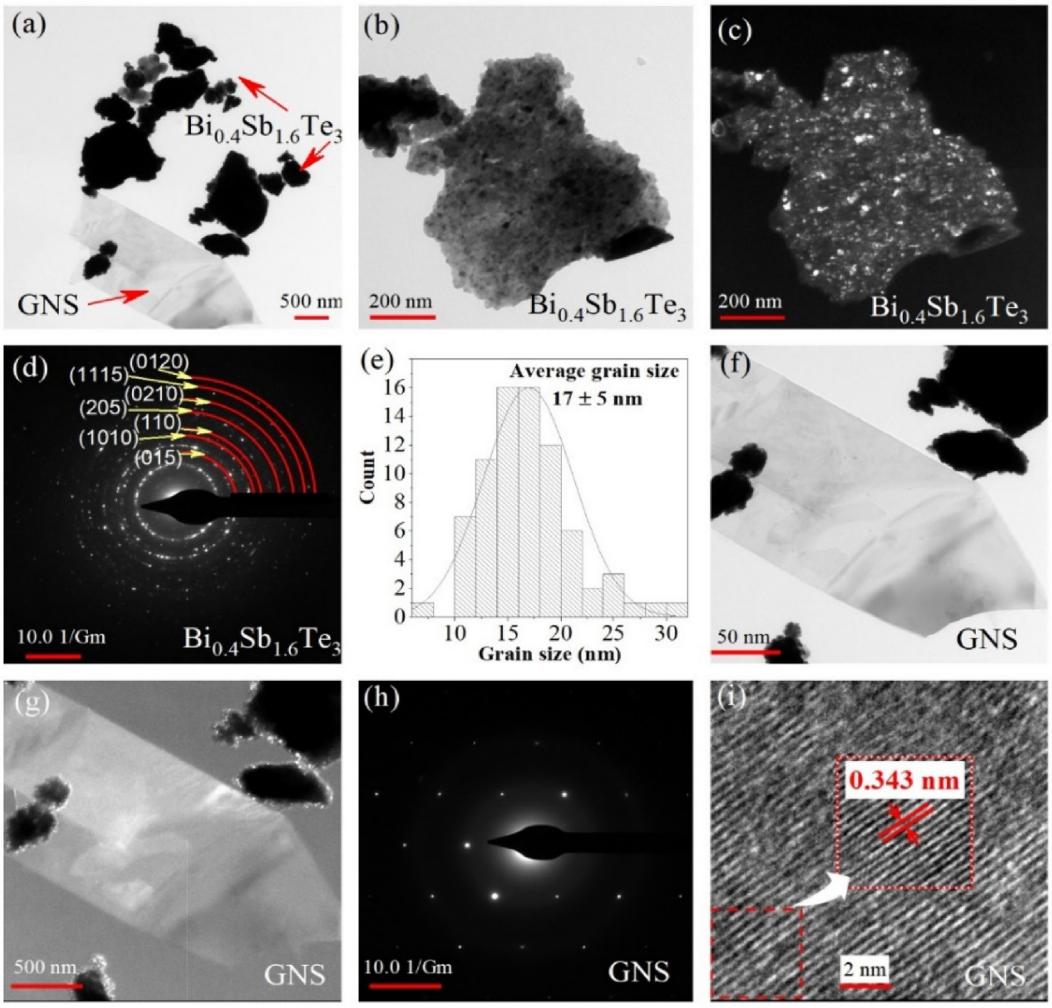

Fig. 4 – TEM analysis for as milled 5m-GNS/$Bi_{0.4}Sb_{1.6}Te_3$ sample showing (a) a bright-field TEM image for the nanocomposite, (b) bright-field, (c) dark-field, (d) diffraction pattern and (e) grain size distribution for the $Bi_{0.4}Sb_{1.6}Te_3$ matrix, and (f) bright-field, (g) dark-field, (h) diffraction pattern and (i) HRTEM image for the GNS filler.

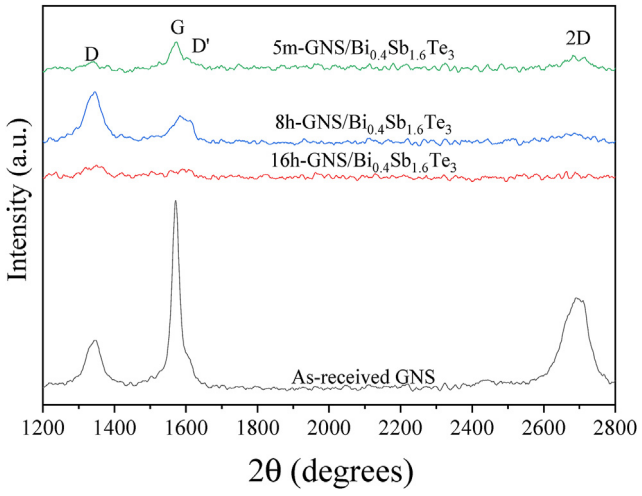

Fig. 5 – The Raman Spectroscopy scans for as-received GNS and GNS/$Bi_{0.4}Sb_{1.6}Te_3$ nanocomposites.

degree of induced structural defects from 0.18 to 2.01 in I_D/I_G ratio. Thus, the delayed addition times of graphene to $Bi_{0.4}Sb_{1.6}Te_3$ nanopowder is favored as it shortens its milling duration to preserve its 2D nanostructure and advantages its exceptional properties.

The evolution of Raman spectra, including the positions and intensities of D, G, 'D', and 2D bands, has been utilized in differentiating graphene from its carbon allotropes (e.g., graphite and carbon nanotubes). Figure 5 shows also the prominent Raman features of the monolayered graphene sheet in the synthesized 5m-GNS/$Bi_{0.4}Sb_{1.6}Te_3$ nanocomposite. The Raman profile of this sample reveals distinguishable peaks at around 1342, 1574, and 2682 cm^{-1} for D, G, and 2D bands, respectively. These peaks are positioned with slight blueshifts of only 0.1, 2, and 8 cm^{-1} from the corresponding ones in the reference graphene. However, these shifts are dramatic in the remained nanocomposites, which are pre-characterized with multilayered graphene.

Table 4 – The intensity ratios and the corresponding number of graphene layers in as-received GNS and GNS/$Bi_{0.4}Sb_{1.6}Te_3$ nanocomposites based on Raman spectra.

Sample	I_D/I_G	I_{2D}/I_G	GNS Layers
as-received GNS	0.26	0.5	multi
16h-GNS/$Bi_{0.4}Sb_{1.6}Te_3$	2.01	0.2	multi
8h-GNS/$Bi_{0.4}Sb_{1.6}Te_3$	1.87	0.5	multi
5m-GNS/$Bi_{0.4}Sb_{1.6}Te_3$	0.18	2.0	single

Additionally, the D-mode signal, which is induced via defects or disorders, appears in the lowest intensity in the 5mins nanocomposite [36]. This indicates the high crystallinity of graphene filler and the absence of new structural defects throughout the compositing process with $Bi_{0.4}Sb_{1.6}Te_3$ nanopowder using the ball milling technique. This allows to preserve the large surface area of the monolayer graphene and then strengthens its interfacial interactions with $Bi_{0.4}Sb_{1.6}Te_3$ nanocrystals. This could be the reason for the nanostructure of the synthesized 5mins nanocomposite. This will return also in a stabilized TE nanocomposite with enhanced matrix and filler interactions for isotropic TE performance.

3.2. *Thermoelectric properties measurements*

The thermoelectric performance of the synthesized TE samples has been tested via the SBA-458 and LFA-467 instruments. The practical design of the SBA-458 has permitted simultaneous measurements of the electrical conductivity (σ) and Seebeck coefficient (S) in the temperature ranges from 323 K to 425 K, as displayed in Fig. 6a and b, respectively. The electrical conductivity of the tested SPS pellets for pristine $Bi_{0.4}Sb_{1.6}Te_3$

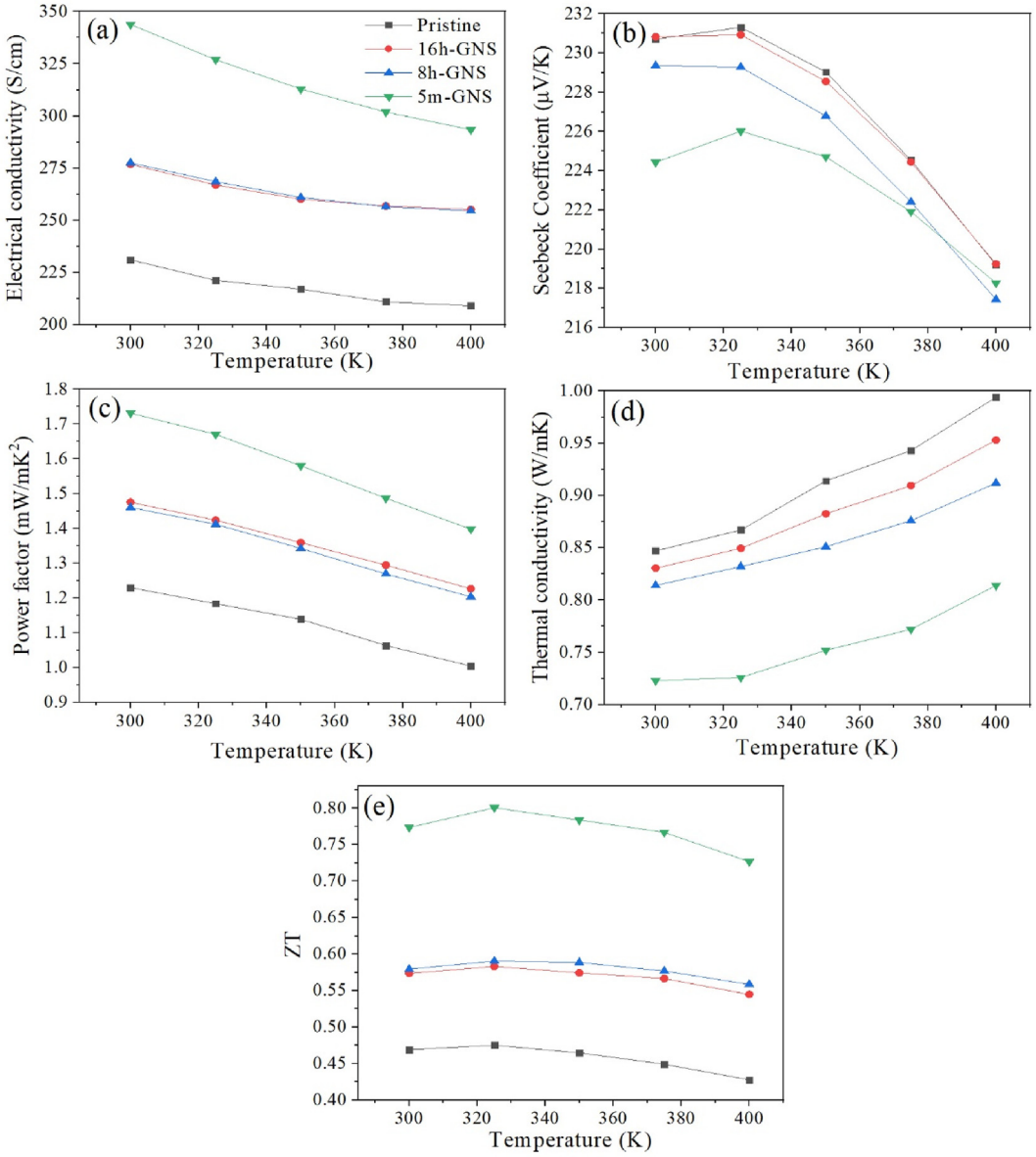

Fig. 6 – The Temperature dependence of thermoelectric properties: (a) electrical conductivity, (b) Seebeck coefficient, (c) power factor, (d) thermal conductivity, and (e) Figure-of-Merits (ZT) for pristine $Bi_{0.4}Sb_{1.6}Te_3$ and GNS/$Bi_{0.4}Sb_{1.6}Te_3$ nanocomposites.

and 0.05wt% GNS/$Bi_{0.4}Sb_{1.6}Te_3$ nanocomposites show a linear decrease with increasing temperature. Their typical behavior matches the metallic behavior at elevated temperatures due to the increased thermal excitations of lattice vibrations [37]. The lattice vibration increases scattering rates via collisions with crystallographic defects, which in turn obstruct the flow of charge carriers, decrease their mean free path, and reduce their mobility [37].

However, this drop in electrical conductivity is not very sharp as it decreases from 231S/cm at 323 K to 209 S/cm at 420 K for the pristine $Bi_{0.4}Sb_{1.6}Te_3$, as shown in Fig. 6a. The addition of graphene to the p-type BiSbTe has impressed the electrical conductivity for all samples at different conditions, as shown in Fig. 6a. It is worth mentioning that the electrical conductivity of pristine $Bi_{0.4}Sb_{1.6}Te_3$ has considerably improved from 231S/cm to 344S/cm at 322 K after compositing it with graphene nanoplatelets. This refers to its high charge carrier density and mobility due to owning a unique 2D nanostructure that offers additional charge transmission channels [38].

On the other hand, the positive values of the Seebeck coefficient confirm the effectiveness in resonant level doping of Bi–Te system with Sb dopant to form the desired p-type $Bi_{0.4}Sb_{1.6}Te_3$, as presented in Fig. 6b. This p-type semiconductor shows an exponential decay in its Seebeck values as the temperature increases from 323 K to 425 K. The pristine $Bi_{0.4}Sb_{1.6}Te_3$ pellet shows the highest Seebeck coefficient values in reverse to its behavior in electrical conductivity. This is due to the inverse and strong interdependence of electrical conductivity and Seebeck coefficient on charge carrier's density [38].

Accordingly, the power factor ($S^2\sigma$), derived from structure–sensitive properties, namely the Seebeck coefficient and electrical conductivity, shows a linear temperature dependence, as displayed in Fig. 6c. It can be seen that the 5m-GNS/$Bi_{0.4}Sb_{1.6}Te_3$ nanocomposite has the highest power factor of 1.73 mW/m.K^2 at 323 K, which slowly decreased to 1.40 mW/m.K^2 at 423 K. These values are the highest reported (to our knowledge) and overcome the solution-derived BiSbTe with a maximum of 9.0 μW/cm.K^2 and ternary alloy ingot of 18.0 μW/cm.K^2 [38,39]. This high-power factor coincides with its exceptional nanostructure evolution. The grain boundaries in its nanostructure have strengthened the energy filtering of minority carriers with low energy.

This maximized its Seebeck coefficient to reach 225 μV/K at 374 K, which is higher than that reported for $Bi_{0.5}Sb_{1.5}Te_3$ pellet produced from the solution route (168 μV/K at 375 K) [40]. Additionally, its preserved 2D nanostructure of graphene nanoplatelets due to its shortened milling durations has maximized its electrical conductivity to 313 S/cm at 371 K. The measured thermal conductivity of synthesized SPS pellets shows a linear increase with temperature, as displayed in Fig. 6d. This thermal conductivity is lowest at the 5mins nanocomposite, which increases from 0.723 W/m.K at 323 K to 0.815 W/m.K at 423 K. This negligible change in its thermal conductivity over a wide temperature range indicates the influence of graphene in improving its phonons scatterings. These scatterings occur primarily at nanograins boundaries of the $Bi_{0.4}Sb_{1.6}Te_3$ and nanointerfaces of the preserved 2D graphene nanoplatelets.

It is worth pointing out that the thermal conductivity values in Fig. 6d are the total contributions of phonons (lattice thermal conductivity) and charge carriers (electronic thermal conductivity). The phonon contribution is dominant in the degenerated semiconductors and has been quantified via subtracting the measured total thermal conductivity from the calculated electronic conductivity using Wiedemann–Franz law [41]. Consequently, the phonons contribution has been diminished extremely in the 5mins nanocomposite and reached a value of 0.598 W/m.K at 423 K. This is much smaller than the 0.705 W/m.K at 423 K in the pristine $Bi_{0.4}Sb_{1.6}Te_3$ pellet and confirms the advantage of graphene nanocomposite in providing additional interfaces for maximizing phonons scattering.

As a result, the Figure-of-Merit (ZT) shows a temperature-dependence profile, which has been derived via dividing the power factor of the SPS pellets by their total thermal conductivity. Interestingly, the ZT profile shows a considerable enhancement in thermoelectric energy conversion of the 5m-GNS/$Bi_{0.4}Sb_{1.6}Te_3$ nanocomposite that achieved 0.801 at 348 K till 398 K, as presented in Fig. 6e. This shows 65% of improvements to the pristine $Bi_{0.4}Sb_{1.6}Te_3$ pellet and 68% to other literature, particularly at 323 K. This TE performance is highly beneficial for several TE applications in hot countries like Qatar, as the typical room temperature at its summer weather is near 324 K (51°C).

This indicates its ability to attain an isotropic thermoelectric performance over a wide temperature range. This coincides also with the pre-observations on its homogenous elemental distribution and stable single phase of its $Bi_{0.4}Sb_{1.6}Te_3$ matrix. This matches the study objectives in sufficiently enhancing the TE performance of synthesized nanocomposites for reliable service and sustainable energy conversion. This confirms the optimized processing conditions of the high-energy milling and SPS in synthesizing artifact-free nanostructured bulk GNS/$Bi_{0.4}Sb_{1.6}Te_3$ nanocomposites with an isotropic TE performance. Thus, resulting in comparable TE performance to other p-type BiTe-based TE materials synthesized via different techniques such as laser 3D printing, chemical reactions, and ingot vibration crashing [42–44].

3.3. *Thermoelectric device modeling*

The investigated method of altering graphene addition time into the mechanical milling process used by our group for the p- and n-types prove that the TE properties are indeed enhanced when GNS is added in the last minutes of the process. To assess the improved TE properties achieved, the samples were modeled using the Thermal-Electric system in ANSYS Workbench software. As explained in the experimental section, the same model was applied for two different systems. System 1: pristine $Bi_{0.4}Sb_{1.6}Te_3$ and $Bi_2Te_{2.7}Se_{0.3}$ alloys, and system 2: optimized GNS based nanocomposites of 5m-GNS/$Bi_{0.4}Sb_{1.6}Te_3$ and 10m-GNS/$Bi_2Te_{2.7}Se_{0.3}$.

For each system, eight source temperatures were tested, which are 30, 40, 70, 100, 150, 200, 250, and 300 °C. Figure 7 a and b show the simulated cases for system 1, with a source temperature of 150 °C. In this system, the simulated model has a maximum current of 1.6 A and an output power of

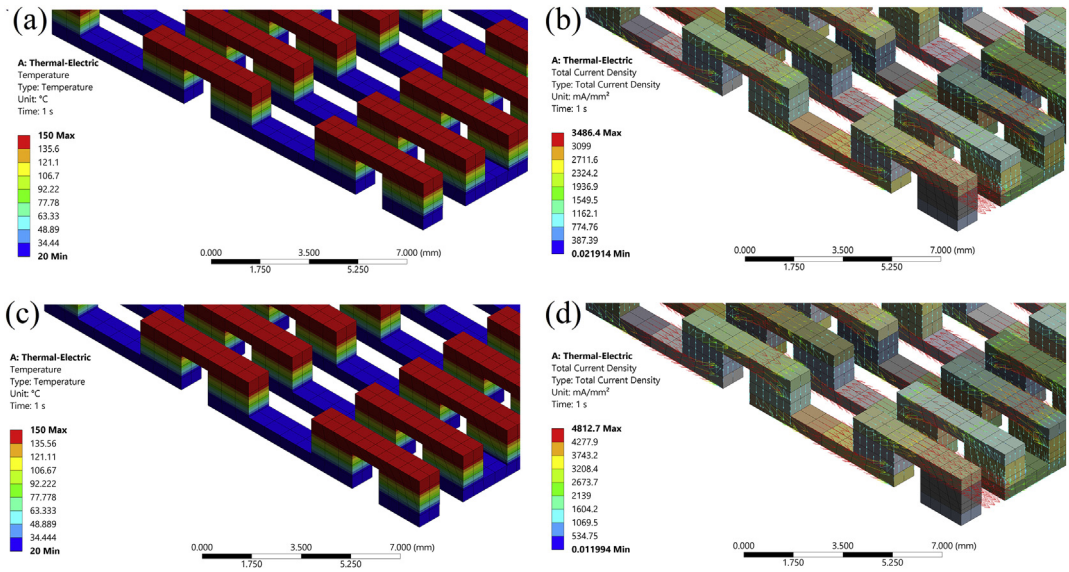

Fig. 7 – The ANSYS TE models for system 1 of pristine $Bi_{0.4}Sb_{1.6}Te_3$ – $Bi_2Te_{2.7}Se_{0.3}$ alloys demonstrating (a) the temperature and (b) the total current density profiles. The TE models for system 2 of 5m-GNS/$Bi_{0.4}Sb_{1.6}Te_3$ and 10m-GNS/$Bi_2Te_{2.7}Se_{0.3}$ nanocomposites with (c) the temperature and (d) the total current density profiles.

89.99 W. The temperature distribution through the device is shown in Fig. 7a. As expected, the maximum temperature is at the top of the thermocouple, while the minimum is at the bottom. Figure 7b demonstrates the total current density vectors within the thermocouple showing the movement of carriers through the device. The same boundary conditions were applied for system 2 (Fig. 7c and d). Similar observations are noticed in the temperature and current density profiles. However, the system records a higher current of 2.2 A and output power of 95.57 W at 150 °C.

The obtained output power of system 1 is 89.95 W, which is higher compared to other studies that simulated bismuth telluride alloys (1–20 W [21], 3–6 W [45], and 0.8–3.6 W [46]). The resulted enhancements in output power could be attributed to the size, arrangements, the number of TE legs, as well the enhanced p- and n-type Bi_2Te_3 materials used in this model. The reason behind adopting this design of TE device is to examine its TE conversion suitability for miniaturized and portable applications such as smartphones, laptops, and other mini self-powered systems. The effect of the applied temperature difference and the GNS addition on the produced power is shown in Fig. 8.

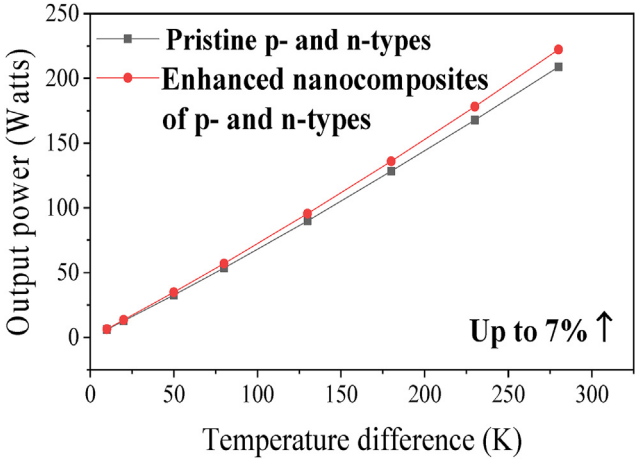

Fig. 8 – Power generated using the two systems of pristine alloys and GNS nanocomposites.

The shown data was obtained for both systems by altering the source temperature while maintaining the sink temperature at 20 °C. It can be observed that the power rises linearly with increasing the temperature difference, matching well with reported trends [22]. Hence, increasing the temperature difference across the device is key to enhancing its efficiency. On another note, GNS addition increased the output power of the device up to 7% compared with using pristine alloys. Even though the resulting enhancement in performance is not dramatically high, increasing the segment builds of the material is expected to show considerable improvements.

4. Conclusions

The graphene enhancements on thermoelectric properties of $Bi_{0.4}Sb_{1.6}Te_3$ alloys for efficient TE energy conversion were studied via a combination of high-energy ball milling and SPS sintering techniques. The structural and morphology of synthesized pristine $Bi_{0.4}Sb_{1.6}Te_3$ and 0.05wt% GNS/$Bi_{0.4}Sb_{1.6}Te_3$ nanocomposites were investigated via XRD, TEM, and Raman. The XRD analysis demonstrated the uniform crystallographic structure and atomic composition of synthesized $Bi_{0.4}Sb_{1.6}Te_3$ nanocrystals in pristine and nanocomposite samples. This confirmed that the 16hrs of mechanical milling was sufficient for synthesizing a single-phase and artifact-free bulk nanocrystalline $Bi_{0.4}Sb_{1.6}Te_3$ into extremely small nanocrystals sizes of 17 nm.

The size of $Bi_{0.4}Sb_{1.6}Te_3$ nanocrystals was consistent with the outcomes of statistical analysis on the DF-TEM micrographs on the 5min nanocomposite. The BF and DF TEM

micrographs of graphene filler in 5min nanocomposite confirmed its mechanical exfoliation during the milling process into a single-layered nanostructure. Its SADP displayed equiaxed and randomly distributed grains within the $Bi_{0.4}Sb_{1.6}Te_3$ matrix in an interplanar spacing of 0.343 nm. The outcomes of the I_{2D}/I_G ratio in Raman analysis highlighted the crucial rule of graphene addition time on its structure and morphology of the synthesized nanocomposites. The excessive milling of graphene due to its addition at early milling times has affected its unique 2D integrity.

This draws a direct relationship between graphene's structural integrity to its milling time. The shortened milling durations are favored to preserve its 2D nanostructure and advantage its exceptional properties. Thus, the prominent Raman features of the monolayered graphene sheet appeared in the synthesized 5m-GNS/$Bi_{0.4}Sb_{1.6}Te_3$ nanocomposite. This allowed to preserve the large surface area of the monolayer graphene and then strengthens its interfacial interactions with $Bi_{0.4}Sb_{1.6}Te_3$ nanocrystals. Thus, the 5m-GNS/$Bi_{0.4}Sb_{1.6}Te_3$ nanocomposite has shown the highest power factor of 1.73 mW/m.K^2 at 323 K. Its thermal conductivity was the lowest with negligible change over a wide temperature range indicating the influence of single-layered graphene in improving its phonons scatterings. These scatterings occurred primarily at nanograins boundaries of the $Bi_{0.4}Sb_{1.6}Te_3$ and nanointerfaces of the preserved 2D graphene nanoplatelets.

The ZT profile of 5m-GNS/$Bi_{0.4}Sb_{1.6}Te_3$ nanocomposite reached 0.801 at 348 K till 398 K. This resulted in 65% of improvements to the pristine $Bi_{0.4}Sb_{1.6}Te_3$ pellet at 323 K. This breakthrough in stabilized TE performance of graphene/$Bi_{0.4}Sb_{1.6}Te_3$ nanocomposites shows sustainable energy conversion for reliable service. The ANSYS Workbench software was used to simulate the standard TE device modules based on pristine $Bi_{0.4}Sb_{1.6}Te_3$–$Bi_2Te_{2.7}Se_{0.3}$ alloys and 5m-GNS/$Bi_{0.4}Sb_{1.6}Te_3$–10m-GNS/$Bi_2Te_{2.7}Se_{0.3}$ nanocomposites. The simulated GNS nanocomposites module at a temperature difference of 150 °C showed a higher generated current of 2.2 A and an output power of 95.5 W compared to that of the pristine module with 1.6 A and 89.9 W. The addition of GNS has enhanced the output power by 7% leading to comparable outcomes to other simulated Bi–Te systems. The modules exhibited a linear relation to the incrementation of source temperature while fixing the sink temperature at 20 °C.

Declaration of Competing Interest

The authors declare that they have no known competing financial interests or personal relationships that could have appeared to influence the work reported in this paper.

Acknowledgments

This work is supported by the Qatar National Research Fund (a member of the Qatar Foundation) from Grant no. NPRP10–0206–170366 and Grant no. GSRA8-L-1-0414-21013. Additional support is also provided from Qatar University Grant no. GTRA-17722. The statements made herein are solely the responsibility of the authors. The authors would like to acknowledge the technical support from the central lab unit and the center of advanced materials at Qatar University. Open Access funding is provided by the Qatar National Library.

REFERENCES

[1] Hou W, Nie X, Zhao W, Zhou H, Mu X, Zhu W, et al. Fabrication and excellent performances of Bi0.5Sb1.5Te3/epoxy flexible thermoelectric cooling devices. Nano Energy 2018;50:766–76. https://doi.org/10.1016/j.nanoen.2018.06.020.

[2] Gelbstein Y, Rosenberg Y, Sadia Y, Dariel MP. Thermoelectric properties evolution of spark Plasma sintered (Ge0.6Pb0.3Sn0.1)Te following a spinodal decomposition; 2010. 13126–31.

[3] Sadia Y, Ohaion-Raz T, Ben-Yehuda O, Korngold M, Gelbstein Y. Criteria for extending the operation periods of thermoelectric converters based on IV-VI compounds. J Solid State Chem 2016;241:79–85. https://doi.org/10.1016/j.jssc.2016.06.006.

[4] Zilber T, Cohen S, Fuks D, Gelbstein Y. TiNiSn half-Heusler crystals grown from metallic flux for thermoelectric applications. J Alloys Compd 2019;781:1132–8. https://doi.org/10.1016/j.jallcom.2018.12.165.

[5] Meroz O, Gelbstein Y. Thermoelectric Bi2Te3-xSex alloys for efficient thermal to electrical energy conversion. Phys Chem Chem Phys 2018;20:4092–9. https://doi.org/10.1039/c7cp06176e.

[6] Sadia Y, Elegrably M, Ben-Nun O, Marciano Y, Gelbstein Y. Submicron features in higher manganese silicide. J Nanomater 2013:5–10. https://doi.org/10.1155/2013/701268. 2013.

[7] Molina-Lopez F. Emerging thermoelectric generators based on printed and flexible electronics technology. Proc IEEE Sensors 2020:1–4. https://doi.org/10.1109/SENSORS47125.2020.9278922. 2020-October.

[8] Zhang C, Peng Z, Li Z, Yu L, Khor KA, Xiong Q. Controlled growth of bismuth antimony telluride $Bi_xSb_{2-x}Te_3$ nanoplatelets and their bulk thermoelectric nanocomposites. Nano Energy 2015;15:688–96. https://doi.org/10.1016/j.nanoen.2015.05.022.

[9] Ojha GP, Pant B, Park SJ, Park M, Kim HY. Synthesis and characterization of reduced graphene oxide decorated with CeO2-doped MnO2nanorods for supercapacitor applications. J Colloid Interface Sci 2017;494:338–44. https://doi.org/10.1016/j.jcis.2017.01.100.

[10] Zhang T, Zhang Q, Jiang J, Xiong Z, Chen J, Zhang Y, et al. Enhanced thermoelectric performance in p-type BiSbTe bulk alloy with nanoinclusion of ZnAlO. Appl Phys Lett 2011;98. https://doi.org/10.1063/1.3541654.

[11] Zhuang HL, Pei J, Cai B, Dong J, Hu H, Sun FH, et al. Thermoelectric performance enhancement in BiSbTe alloy by microstructure modulation via cyclic spark Plasma sintering with liquid phase. Adv Funct Mater 2021:31. https://doi.org/10.1002/adfm.202009681.

[12] He J, Kanatzidis MG, Dravid VP. High performance bulk thermoelectrics via a panoscopic approach. Mater Today 2013;16:166–76. https://doi.org/10.1016/j.mattod.2013.05.004.

[13] Suh D, Lee S, Mun H, Park SH, Lee KH, Wng Kim S, et al. Enhanced thermoelectric performance of Bi0.5Sb1.5Te3-expanded graphene composites by simultaneous modulation of electronic and thermal carrier transport. Nano Energy 2015;13:67–76. https://doi.org/10.1016/j.nanoen.2015.02.001.

[14] Zebarjadi M, Esfarjani K, Dresselhaus MS, Ren ZF, Chen G. Perspectives on thermoelectrics: from fundamentals to device applications. Energy Environ Sci 2012;5:5147–62. https://doi.org/10.1039/c1ee02497c.

[15] Lemine AS, Zagho MM, Altahtamouni TM, Bensalah N. Graphene a promising electrode material for supercapacitors—a review. Int J Energy Res 2018;42:4284–300. https://doi.org/10.1002/er.4170.
[16] Chakraborty P, Ma T, Zahiri AH, Cao L, Wang Y. Carbon-based materials for thermoelectrics. Adv Condens Matter Phys 2018;2018. https://doi.org/10.1155/2018/3898479. 2018.
[17] Tang X, Xie W, Li H, Zhao W, Zhang Q, Niino M. Preparation and thermoelectric transport properties of high-performance p-type Bi2Te3 with layered nanostructure. Appl Phys Lett 2007;90:1–4. https://doi.org/10.1063/1.2425007.
[18] Chen S, Cai W, Piner RD, Suk JW, Wu Y, Ren Y, et al. Synthesis and characterization of large-area graphene and graphite. Nano Lett 2011:3519–25. https://doi.org/10.3969/j.issn.1001-9731.2013.09.030.
[19] Xie D, Xu J, Liu G, Liu Z, Shao H, Tan X, et al. Synergistic optimization of thermoelectric performance in p-type Bi0.48Sb1.52Te3/graphene composite. Energies 2016;9:1–9. https://doi.org/10.3390/en9040236.
[20] Antonova EE, Looman DC. Finite elements for thermoelectric device analysis in ANSYS. Int Conf Thermoelectr ICT, Proc 2005:200–3. https://doi.org/10.1109/ICT.2005.1519922. 2005.
[21] Kondaguli RS, Malaji PV. Analysis of bismuth telluride (Bi2Te3) thermoelectric generator. Proc B-HTC 2020 - 1st IEEE Bangalore Humanit Technol Conf 2020. https://doi.org/10.1109/B-HTC50970.2020.9297843.
[22] Seetawan T, Seetawan U, Ratchasin A, Srichai S, Singsoog K, Namhongsa W, et al. Analysis of thermoelectric generator by finite element method. Procedia Eng 2012;32:1006–11. https://doi.org/10.1016/j.proeng.2012.02.046.
[23] El-Makaty FM, Andre Mkhoyan K, Youssef KM. The effects of structural integrity of graphene on the thermoelectric properties of the n-type bismuth-telluride alloy. J Alloys Compd 2021;876:160198. https://doi.org/10.1016/j.jallcom.2021.160198.
[24] Degen T, Sadki M, Bron E, König U, Nénert G. The high score suite. Powder Diffr 2014;29:S13–8. https://doi.org/10.1017/S0885715614000840.
[25] Wang YS, Huang LL, Li D, Zhang J, Qin XY. Enhanced thermoelectric performance of Bi0.4Sb1.6Te3based composites with CuInTe2inclusions. J Alloys Compd 2018;758:72–7. https://doi.org/10.1016/j.jallcom.2018.05.035.
[26] Waguespack L, Blaine R. Design of a new DSC cell with tzero ™ technology. Proc 29th Conf North Am Therm Anal Soc 2001:721–7.
[27] Youssef KM, Scattergood RO, Murty KL, Koch CC. Nanocrystalline Al-Mg alloy with ultrahigh strength and good ductility. Scripta Mater 2006;54:251–6. https://doi.org/10.1016/j.scriptamat.2005.09.028.
[28] Choi H, Kim YJ, Kim CS, Yang HM, Oh MW, Cho BJ. Enhancement of reproducibility and reliability in a high-performance flexible thermoelectric generator using screen-printed materials. Nano Energy 2018;46:39–44. https://doi.org/10.1016/j.nanoen.2018.01.031.
[29] Ahmad SI, Hamoudi H, Ponraj J, Youssef KM. In-situ growth of single-crystal plasmonic aluminum–lithium-graphene nanosheets with a hexagonal platelet-like morphology using ball-milling. Carbon N Y 2021;178:657–65. https://doi.org/10.1016/j.carbon.2021.03.053.
[30] Bastwros M, Kim GY, Zhu C, Zhang K, Wang S, Tang X, et al. Effect of ball milling on graphene reinforced Al6061 composite fabricated by semi-solid sintering. Compos B Eng 2014;60:111–8. https://doi.org/10.1016/j.compositesb.2013.12.043.
[31] Liang A, Jiang X, Hong X, Jiang Y, Shao Z, Zhu D. Recent developments concerning the dispersion methods and mechanisms of graphene. Coatings 2018;8. https://doi.org/10.3390/coatings8010033.
[32] Ju H, Kim J. The effect of temperature on thermoelectric properties of n-type Bi2Te3 nanowire/graphene layer-by-layer hybrid composites. Dalton Trans 2015;44:11755–62. https://doi.org/10.1039/c5dt00897b.
[33] Shin WH, Ahn K, Jeong M, Yoon JS, Song JM, Lee S, et al. Enhanced thermoelectric performance of reduced graphene oxide incorporated bismuth-antimony-telluride by lattice thermal conductivity reduction. J Alloys Compd 2017;718:342–8. https://doi.org/10.1016/j.jallcom.2017.05.204.
[34] Gao G, Liu D, Tang S, Huang C, He M, Guo Y, et al. Heat-initiated chemical functionalization of graphene. Sci Rep 2016;6:1–9. https://doi.org/10.1038/srep20034.
[35] Antonio C, Cuevas C, Esparza R. Materials characterization series 1994. https://doi.org/10.1016/b978-0-7506-9386-8.50001-0.
[36] Nolas GS, Poon J. R ecent Developments Thermoelectric Materials 2016;31:199–205.
[37] Ahmad K, Wan C, Zong P an. Thermoelectric properties of BiSbTe/graphene nanocomposites. J Mater Sci Mater Electron 2019;30:11923–30. https://doi.org/10.1007/s10854-019-01538-z.
[38] Zhang D, Lei J, Guan W, Ma Z, Wang C, Zhang L, et al. Enhanced thermoelectric performance of BiSbTe alloy: energy filtering effect of nanoprecipitates and the effect of SiC nanoparticles. J Alloys Compd 2019:1276–83. https://doi.org/10.1016/j.jallcom.2019.01.084.
[39] Chen L, Mei D, Wang Y, Li Y. Ni barrier in Bi2Te3-based thermoelectric modules for reduced contact resistance and enhanced power generation properties. J Alloys Compd 2019;796:314–20. https://doi.org/10.1016/j.jallcom.2019.04.293.
[40] Dou YC, Qin XY, Li D, Li YY, Xin HX, Zhang J, et al. Enhanced thermoelectric performance of BiSbTe-based composites incorporated with amorphous Si_3N_4 nanoparticles. RSC Adv 2015;5:34251–6. https://doi.org/10.1039/c5ra04428f.
[41] Parker D, Singh DJ. Potential thermoelectric performance from optimization of hole-doped Bi2Se3. Phys Rev X 2011;1:1–9. https://doi.org/10.1103/PhysRevX.1.021005.
[42] Min Y, Roh JW, Yang H, Park M, Kim S Il, Hwang S, et al. Surfactant-free scalable synthesis of Bi2Te3 and Bi2Se3 nanoflakes and enhanced thermoelectric properties of Their Nanocomposites. Adv Mater 2013;25:1425–9. https://doi.org/10.1002/adma.201203764.
[43] Hu X, Xiang Q, Kong D, Fan X, Feng B, Pan Z, et al. The effect of Ni/Sn doping on the thermoelectric properties of BiSbTe polycrystalline bulks. J Solid State Chem 2019;277:175–81. https://doi.org/10.1016/j.jssc.2019.06.006.
[44] Qiu J, Yan Y, Luo T, Tang K, Yao L, Zhang J, et al. 3D Printing of highly textured bulk thermoelectric materials: mechanically robust BiSbTe alloys with superior performance. Energy Environ Sci 2019;12:3106–17. https://doi.org/10.1039/c9ee02044f.
[45] Picard M, Turenne S, Vasilevskiy D, Masut RA. Numerical simulation of performance and thermomechanical behavior of thermoelectric modules with segmented bismuth-telluride-based legs. J Electron Mater 2013;42:2343–9. https://doi.org/10.1007/s11664-012-2435-5.
[46] Cheng F, Hong Y, Zhong W, Zhu C. Performance prediction and test of a Bi2Te3-based thermoelectric module for waste heat recovery. J Therm Anal Calorim 2014;118:1781–8. https://doi.org/10.1007/s10973-014-4153-0.